Geophysical Journal International

*Geophys. J. Int.* (2020) **223,** 1054–1068
Advance Access publication 2020 July 21
GJI Seismology

doi: 10.1093/gji/ggaa350

# Source modelling and strong ground motion simulations for the 24 January 2020, $M_w$ 6.8 Elazığ earthquake, Turkey

Daniele Cheloni and Aybige Akinci

*Istituto Nazionale di Geofisica e Vulcanologia, Via di Vigna Murata* 605, 00143 Roma, *Italy. E-mail: daniele.cheloni@ingv.it*

Accepted 2020 July 18. Received 2020 June 23; in original form 2020 May 4

## SUMMARY

On 24 January 2020 an $M_w$ 6.8 earthquake occurred at 20:55 local time (17:55 UTC) in eastern Turkey, close to the town of Sivrice in the Elazığ province, causing widespread considerable seismic damage in buildings. In this study, we analyse the main features of the rupture process and the seismic ground shaking during the Elazığ earthquake. We first use Interferometric Synthetic Aperture Radar (InSAR) interferograms (Sentinel-1 satellites) to constrain the fault geometry and the coseismic slip distribution of the causative fault segment. Then, we utilize this information to analyse the ground motion characteristics of the main shock in terms of peak ground acceleration (PGA), peak ground velocity (PGV) and spectral accelerations. The absence of seismic registrations in near-field for this earthquake imposes major constraints on the computation of seismic ground motion estimations in the study area. To do this, we have used a stochastic finite-fault simulation method to generate high-frequency ground motions synthetics for the $M_w$ 6.8 Elazığ 2020 earthquake. Finally, we evaluate the potential state of stress of the unruptured portions of the causative fault segment as well as of adjacent segments, using the Coulomb stress failure function variations. Modelling of geodetic data shows that the 2020 Elazığ earthquake ruptured two major slip patches (for a total length of about 40 km) located along the Pütürge segment of the well-known left-lateral strike-slip East Anatolian Fault Zone (EAFZ), with up to 2.3 m of slip and an estimated geodetic moment of $1.70 \times 10^{19}$ Nm (equivalent to a $M_w$ 6.8). The position of the hypocentre supports the evidence of marked WSW rupture directivity during the main shock. In terms of ground motion characteristics, we observe that the high-frequency stochastic ground motion simulations have a good capability to reproduce the source complexity and capture the ground motion attenuation decay as a function of distance, up to the 200 km. We also demonstrate that the design spectra corresponding to 475 yr return period, provided by the new Turkish building code is not exceeded by the simulated seismograms in the epicentral area where there are no strong motion stations and no recordings available. Finally, based on the Coulomb stress distribution computation, we find that the Elazığ main shock increased the stress level of the westernmost part of the Pütürge fault and of the adjacent Palu segment and as a result of an off-fault lobe.

**Key words:** Radar interferometry; Europe; Numerical modelling; Earthquake ground motions; Earthquake hazards; Earthquake source observations; Seismic attenuation.

## 1 INTRODUCTION

An earthquake of $M_w$ 6.8 occurred in the Elazığ region of eastern Turkey on 24 January 2020 at 20:55 local time (17:55 UTC), causing loss of life and severe damage in the epicentral area. According to the information provided by the Earthquake Department of the Disaster and Emergency Management Presidency, AFAD, there were 46 reported fatalities and over 1600 injuries in Elazığ, Malatya and Diyarbakir. There are an estimated 10 000 people homeless at this time, sheltering in containers, tents and public refuge sites in schools, sports facilities and dorms. The earthquake was reported to be on a segment of the ∼580-km-long left-lateral continental strike-slip East Anatolian Fault Zone (EAFZ), which is one of the two major active strike-slip fault systems in Turkey, other being the ∼1500-km-long right-lateral strike-slip North Anatolian Fault Zone (NAFZ, inset Fig. 1). The earthquake epicentre is provided by the different national and international Institutes (including AFAD, KOERI, USGS, INGV, GCMT, CPPT, ERD, IPGP, GFZ and EMSC) with rather different locations (in this work we use both the hypocentre information of the main shock based on solution from AFAD and from the Kandilli Observatory and Earthquake Research Institute, KOERI, respectively); however, the magnitude has been assessed

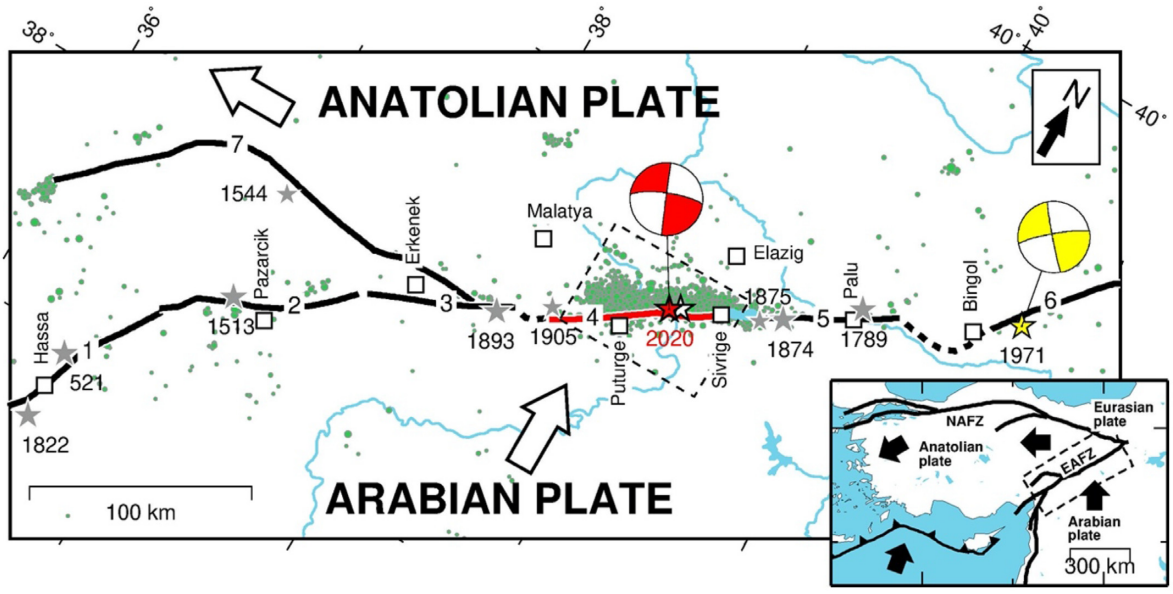


**Figure 1.** Seismotectonic framework of the study area. The solid lines represent the main fault segments of the East Anatolian Fault Zone (EAFZ) with labelled name: (1) Amanos, (2) Pazarcik, (3) Erkenek, (4) Pütürge, (5) Palu and (6) Ilica fault segments, respectively (after Duman & Emre 2013); the red line is the fault segment activated during the 2020 Elazığ seismic sequence; the dashed lines are the related fault jogs. Seismicity: the green circles are the aftershocks of the first 3 months after the main shock (available at https://deprem.afad.gov.tr); the red and white star represent the location of the main shock provided by AFAD and KOERI, respectively, and its moment tensor solution (U.S. Geological Survey 2020); the grey and yellow stars are the location of the source of the major ($M > 6.6$) historical and instrumental earthquakes, respectively, in the region with labelled events date (Ambraseys 1989; Ambraseys & Jackson 1998; Kondorskaya & Ulomov 1999) and their moment tensor solutions (Taymaz *et al.* 1991). The white arrows represent the direction of plate motion. The dashed box highlights the area of Fig. 4. The main map is displayed in an oblique Mercator projection with the equator azimuth parallel to the trend of the EAFZ. The inset shows the main fault systems in and around Turkey (modified from Cetin *et al.* 2003): NAFZ is the North Anatolian Fault Zone; EAFZ is the East Anatolian Fault Zone. Arrows indicate relative plate motions. The dashed box is the area of the main figure.

as $M_w$ 6.7 or 6.8. Its epicentre was located in the Elazığ province, at a distance of about 10–20 km WSW of the Lake Hazar (Fig. 1). Its focal depth ranged from 8 to 23 km. The focal mechanism solution (Fig. 1) indicated that the earthquake is in agreement with the activation of a ENE–WSW striking left-lateral strike-slip fault. The affected area is still experiencing repeated aftershocks, with over 1200 events of magnitude greater than 2.0 within 4 months; 31 aftershocks have been equal to or larger than $M$ 4.0. The largest aftershocks occurred on 25 January, 19 March and 5 June 2020, and their magnitudes have been assessed as $M_w$ 5.1, 5.0 and 5.0, respectively (earthquakes solutions available at https://deprem.afad.gov.tr). Aftershocks spread along a 50–60 km stretch of the EAFZ between Sivrice to Pütürge, both ENE and WSW of the hypocentre, spreading outward from the 30 km section of fault that ruptured on 24 January 2020 (Fig. 1).

In this study, great effort has been directed towards understanding the characteristics of source and ground motion associated with the Elazığ seismic sequence. In this respect, we first use Sentinel-1 Synthetic Aperture Radar (SAR) data to investigate the ground displacement field and to infer, by using elastic dislocation modelling, the fault geometry and slip distribution of the causative fault segment. Then, we performed simulations aiming at reproducing the high-frequency portion of the strong ground motion records obtained during 2020 Elazığ earthquake using the stochastic finite-fault simulation method based on a dynamic corner frequency approach (Motazedian & Atkinson 2005; Boore 2009). The earthquake's complex nature and the sparse strong motion network in the epicentral area makes difficult to define the characteristics of ground shaking particularly in the near-source region. The estimation of ground motions becomes therefore necessary and essential through the earthquake scenarios and several physics-based deterministic, stochastic and hybrid methods (Boore 2003; Motazedian & Atkinson 2005; Graves & Pitarka 2010; Mai *et al.* 2010; Irikura & Miyake 2011; Mena *et al.* 2012; Akinci *et al.* 2017; Pitarka *et al.* 2017, 2019).

The strong ground motion records of Elazığ earthquake were available and provided recently by AFAD that manage the national strong motion network in Turkey. The ground motion parameters in terms of PGA and PGV values and recorded seismograms at 43 strong motion stations within a distance of 200 km from the epicentre are used in this study (Table 1). The observed peak ground accelerations (PGA) were 293 and 239 cm s$^{-2}$, with the highest maxima recorded by the two strong motion stations closest to the fault (within 10 km of the rupture). These stations are located near the epicentre (Sivrice and Pütürge stations, located ∼3 km to the north and ∼6 km to the southeast of the epicentre, respectively), as well as locations that were in the heavily damaged area. Therefore, the simulated ground motions calculated at the 1066 virtual stations distributed on a regular grid with 5 km spacing are validated with the observed ground motion parameters in terms of PGA and PGV values, and then compared with ground motion prediction equations (GMPEs) for epicentral distances up to 200 km.

Finally, because the stress changes in the region due to this earthquake may interact with other fault segments of the EAFZ in the area, in this study, we investigate the static Coulomb stress changes induced by the main shock, by examining both the contribution to the observed aftershock triggering during the 2020 Elazığ sequence and to the adjacent fault segments loading.

**Table 1.** Peak ground accelerations and velocities from the processed recordings of the 2020 Elazığ earthquake, Turkey, on the strong motion stations up to 150 km distances and local site conditions is defined in Eurocode 8 (EC 8: Seismic Design of Buildings).

| Station code | Station name | Station Lat. | Station Lon. | PGA-NS (gal) | PGA-EW (gal) | PGA-Z (gal) | PGV-NS ($ms^{-1}$) | PGV-EW ($ms^{-1}$) | Distance $R_{jb}$ | $V_{S30}$ ($ms^{-1}$) Site EC8 |
|---|---|---|---|---|---|---|---|---|---|---|
| 2308 | Sivrice | 38.45 | 39.31 | 235.78 | 292.80 | 178.57 | 27.81 | 45.34 | 2.63 | 450-B |
| 4404 | Pütürge | 38.20 | 38.87 | 193.59 | 228.44 | 110.62 | 24.82 | 28.71 | 6.16 | 1380-A |
| 2301 | Merkez | 38.67 | 39.19 | 118.92 | 142.61 | 66.24 | 12.35 | 8.75 | 21.95 | 407-B |
| 0204 | Gerger | 38.03 | 39.03 | 94.24 | 110.40 | 59.83 | 17.10 | 9.72 | 29.09 | 555-B |
| 0212 | Sincik | 38.03 | 38.62 | 43.52 | 38.52 | 31.83 | 7.13 | 4.80 | 28.64 | - |
| 2302 | Maden | 38.39 | 39.68 | 25.55 | 31.36 | 22.77 | 3.61 | 2.29 | 33.92 | 907-A |
| 2104 | Ergani | 38.26 | 39.76 | 26.75 | 25.61 | 24.11 | 3.12 | 3.87 | 45.17 | - |
| 4401 | Merkez | 38.35 | 38.34 | 73.23 | 87.63 | 37.35 | 7.74 | 6.91 | 39.96 | 481-B |
| 0205 | Kahta | 37.79 | 38.62 | 25.49 | 41.01 | 26.02 | 6.81 | 7.38 | 52.34 | 660-B |
| 0207 | Çelikhan | 38.03 | 38.25 | 32.94 | 30.50 | 18.18 | 5.06 | 4.27 | 63.36 | 660-B |
| 2304 | Kovancılar | 38.72 | 39.86 | 8.823 | 13.74 | 5.81 | 2.05 | 2.13 | 67.57 | 489.B |
| 4412 | Yazıhan | 38.60 | 38.18 | 21.46 | 18.97 | 14.44 | 4.41 | 4.43 | 62.90 | - |
| 4407 | Arguvan | 38.78 | 38.26 | 31.04 | 23.27 | 20.13 | 3.00 | 4.55 | 70.09 | 735-B |
| 2307 | Palu | 38.70 | 39.93 | 12.81 | 20.82 | 11.88 | 3.74 | 3.00 | 67.57 | 329-C |
| 2105 | Dicle | 38.36 | 40.07 | 10.37 | 11.09 | 8.91 | 1.23 | 1.70 | 68.69 | - |
| 6201 | Merkez | 39.07 | 39.53 | 11.99 | 9.70 | 9.91 | 1.26 | 1.21 | 70.39 | - |
| 0210 | Merkez | 37.77 | 38.29 | 23.04 | 27.43 | 18.04 | 8.27 | 5.48 | 70.09 | - |
| 4406 | Akcadağ | 38.34 | 37.97 | 23.60 | 24.02 | 14.06 | 2.07 | 4.14 | 71.16 | 815-A |
| 0201 | Merkez | 37.76 | 38.27 | 35.9 | 44.61 | 35.14 | 10.08 | 8.10 | 71.15 | 391-B |
| 0209 | Samsat | 37.58 | 38.48 | 70.84 | 58.44 | 24.71 | 4.45 | 4.80 | 77.42 | - |
| 2305 | Beyhan | 38.73 | 40.13 | 3.64 | 4.78 | 4.00 | 0.99 | 1.21 | 80.54 | 907-A |
| 4408 | Doğanşehir | 38.10 | 37.89 | 11.35 | 16.24 | 15.55 | 3.00 | 2.86 | 81.16 | 654-B |
| 2306 | Karakocan | 38.96 | 40.04 | 4.356 | 5.41 | 2.89 | 1.12 | 1.52 | 86.63 | 663-B |
| 4405 | Hekimhan | 38.81 | 37.94 | 11.56 | 11.59 | 6.67 | 4.44 | 1.68 | 94.12 | 579-B |
| 2101 | Bağlar | 37.93 | 40.20 | 24.64 | 26.38 | 13.64 | 2.23 | 2.75 | 97.07 | 519-B |
| 2409 | Kemaliye | 39.28 | 38.49 | 13.71 | 20.43 | 7.04 | 2.79 | 1.73 | 109.83 | 875-A |
| 0213 | Tut | 37.80 | 37.93 | 34.95 | 30.86 | 14.43 | 6.04 | 6.86 | 91.63 | - |
| 6304 | Bozova | 37.37 | 38.51 | 49.02 | 77.71 | 29.94 | 3.60 | 3.17 | 100.24 | 376-B |
| 2415 | İliç | 39.46 | 38.55 | 11.30 | 12.26 | 8.99 | 3.13 | 1.92 | 124.97 | 444-B |
| 4410 | Kuluncak | 38.87 | 37.68 | 13.30 | 15.15 | 6.64 | 2.69 | 1.51 | 116.20 | - |
| 2408 | Kemah | 39.60 | 39.03 | 12.08 | 16.46 | 12.08 | 2.69 | 2.17 | 126.10 | 416-B |
| 2106 | Lice | 38.46 | 40.65 | 8.71 | 10.57 | 8.71 | 1.08 | 1.30 | 118.55 | - |
| 4409 | Darende | 38.56 | 37.49 | 7.91 | 6.95 | 6.68 | 1.03 | 1.24 | 117.11 | - |
| 0208 | Golbasi | 37.79 | 37.65 | 18.06 | 12.42 | 7.62 | 3.38 | 4.31 | 113.26 | 469-B |
| 6302 | Viranşehır | 37.23 | 39.75 | 16.93 | 14.05 | 9.39 | 1.74 | 1.81 | 136.26 | 936-A |
| 6202 | Pülümür | 39.49 | 39.90 | 8.26 | 6.54 | 3.66 | 1.46 | 0.99 | 125.04 | - |
| 2412 | Çağlayan | 39.59 | 39.69 | 2.56 | 2.43 | 1.70 | 0.52 | 0.74 | 129.21 | 955-A |
| 1213 | Adakli | 39.23 | 40.48 | 8.26 | 6.54 | 3.66 | 2.08 | 1.14 | 149.50 | - |

## 2 TECTONIC SETTING, SEISMOTECTONIC AND SEISMICITY

Two major faults contribute to the majority of the seismic hazard in the region, the North Anatolian Fault Zone (NAFZ) and the Eastern Anatolian Fault Zone (EAFZ, Fig. 1). Many large earthquakes have occurred along these faults (Ambraseys 1989) as a result of the ongoing movement between the Eurasian, African, Arabian and Anatolian plates. The NAFZ with right-lateral faulting is extending from Istanbul in the west to Karlıova in the east. During the twentieth century this fault zone has produced many large earthquakes with surface rupturing and with a westward migrating sequence (Barka & Kandinsky-Cade 1988). Around the Karlıova region, NAFZ joins the SW-trending EAFZ.

The EAFZ forms a ∼580 km left-lateral strike-slip transform boundary between the northward moving Arabian Plate and westward moving Anatolian block (Fig. 1), resulting in a left-lateral slip rate of $\sim 10 \pm 1$ mm yr$^{-1}$ on the EAFZ (e.g. McClusky *et al.* 2000; Reilinger *et al.* 2006; Aktug *et al.* 2016), but its faulting is less continuous and less localized than that of the NAFZ (Ambraseys 2009). In fact, the EAFZ constitutes a complex left-lateral strike-slip fault zone and it is divided into a number of fault segments (Fig. 1), as suggested by different authors based on variations in trends, location of geometric discontinuities, extent of surface ruptures, stepovers and bend structures along the EAFZ, mapping of active faults, seismological and palaeoseismological data (e.g. Hempton *et al.* 1981; Barka & Kadinsky-Cade 1988; Saroglu *et al.* 1992; Herece 2008; Duman & Emre 2013). According to Duman & Emre (2013), from SW to NE, the fault segments of the main EAFZ fault strand are: the Amanos, Pazarcık, Erkenek, Pütürge, Palu, Ilıca and Karlıova segments (Fig. 1). The length of these fault segments varies from 31 to 112 km, while their strikes vary from N35° E to N75° E (Duman & Emre 2013).

Since this zone is tectonically very active, a series of large surface rupturing earthquakes occurred along the EAFZ main strand during the last centuries (Fig. 1). From NE to SW the following large earthquakes have occurred: the 1866 earthquake of $M_s$ 7.0 that can be correlated to the Karlıova segment (Ambraseys & Jackson 1998); the 1971 Bingöl earthquake of $M_s$ 6.8 occurred between Karlıova and Bingöl (McKenzie 1972); the 1874 earthquake of $M_s$ 7.1 occurred on the Palu segment (Ambraseys & Jackson 1998;

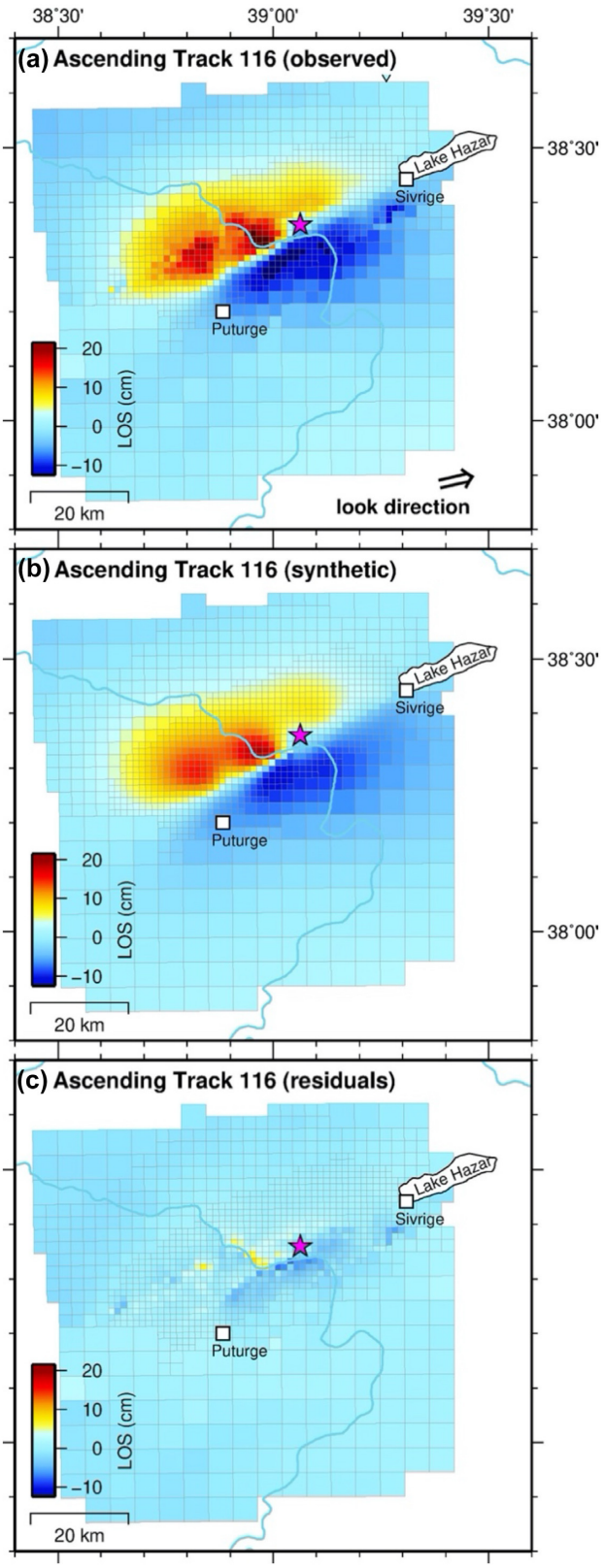


**Figure 2.** (a) Data, (b) model and (c) residual sampled points from the unwrapped interferogram showing the coseismic displacement field from the Sentinel-1 ascending track 116. The pink star indicates the main shock epicentre provided by AFAD.

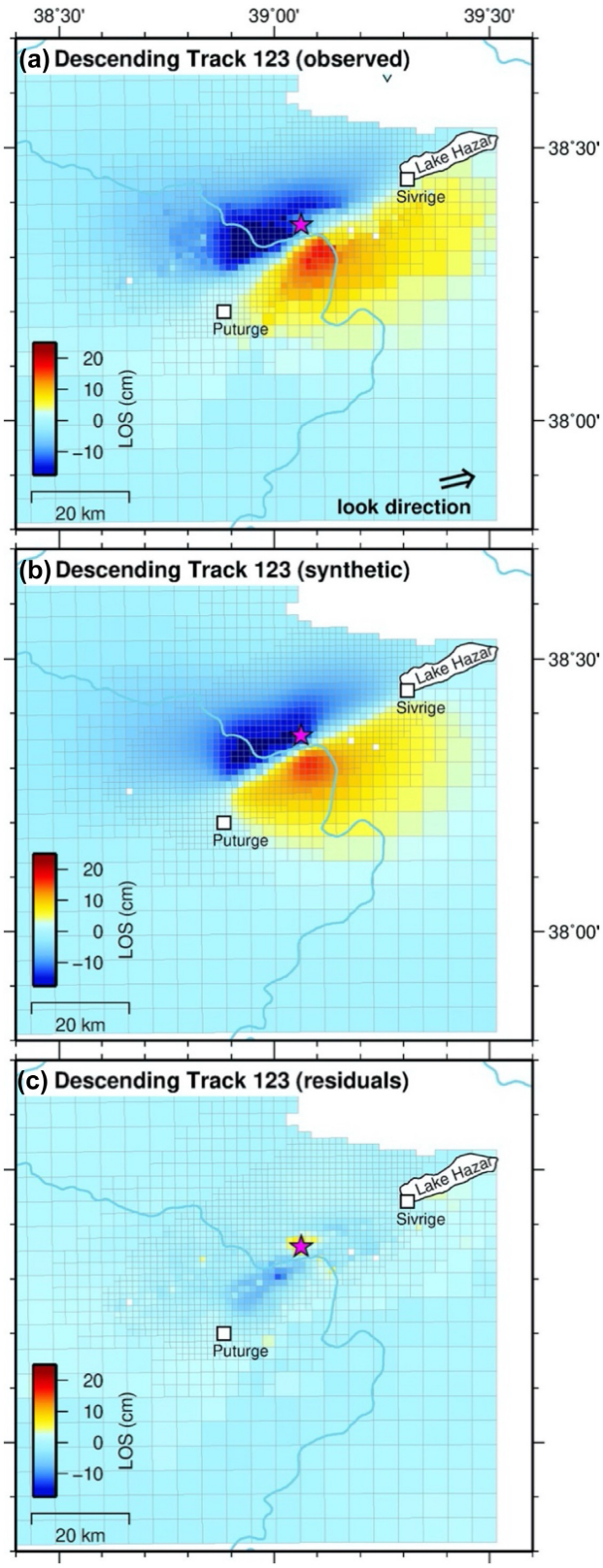


**Figure 3.** (a) Data, (b) model and (c) residual sampled points from the unwrapped interferogram showing the coseismic displacement field from the Sentinel-1 descending track 123. The pink star indicates the main shock epicentre provided by AFAD.

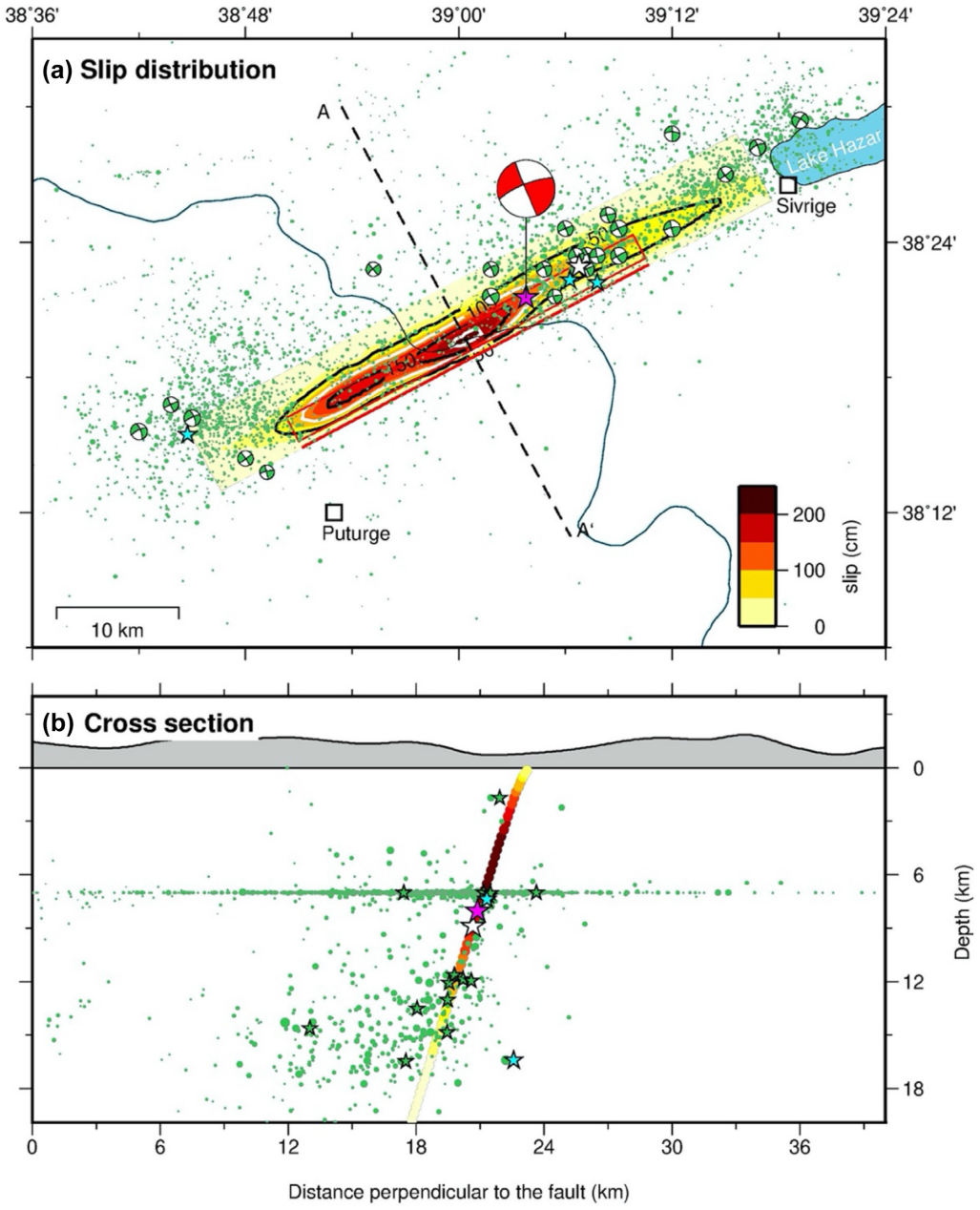


**Figure 4.** (a) Coseismic slip distribution on the Pütürge segment of the EAFZ. The contouring (in cm) indicates the major retrieved coseismic patches of slip. The pink and white stars are the AFAD and KOERI locations of the main shock, respectively; the white blue stars are the major aftershocks with $M > 5$. The red beach ball indicates the mechanisms of the main shock, while the green beach balls are the $M > 4$ aftershocks that occurred in the first 3 months from the main shock. Green circles are aftershocks between 23 January and 23 April. The red box represents our best-fitting uniform slip solution. (b) Estimated slip distribution as a function of depth (symbols as in the top panel). The white blue and green stars are, respectively, the major aftershocks with $M > 5$ and $M > 4$. Note that many hypocentres were located at a fixed depth of 7 km from the automatic AFAD location.

Cetin *et al.* 2003); the 1875 ($M_s$ 6.7) that might have been generated along the easternmost termination of the Pütürge segment (Ambraseys 1989; Cetin *et al.* 2003) or within the complex releasing bend geometry that is inferred to exist within Lake Hazar (Duman & Emre 2013); the 1905 ($M_s$ 6.8) earthquake occurred on the Yarpuzlu restraining bend which is located at the western tip of the Pütürge segment (Ambraseys 1989); the 1893 earthquake of $M_s$ 7.2 occurred on the Erkenek segment (Ambraseys & Jackson 1998); the 1513 earthquake of $M_s$ 7.4 has been attributed to the Pazarcık segment (Herece 2008); the 1822 earthquake of $M$ 7.5 that might have been generated on the Amonos fault segment (Ambraseys & Jackson 1998; Seyrek *et al.* 2007).

Prior to the 24 January 2020 Elazığ earthquake sequence, taking account of the time elapsed from the last event, the slip rate, seismological and palaeoseismological data, some authors have identified some important seismic gaps along the main strand of the EAFZ, the ∼80-km-long Pazarcık (Nalbant *et al.* 2002; Karabacak *et al.* 2011), the ∼100-km-long Amanos and the ∼95-km-long Pütürge segments (Duman & Emre 2013; Aktug *et al.* 2016, Fig. 1). According to these authors these fault segments have

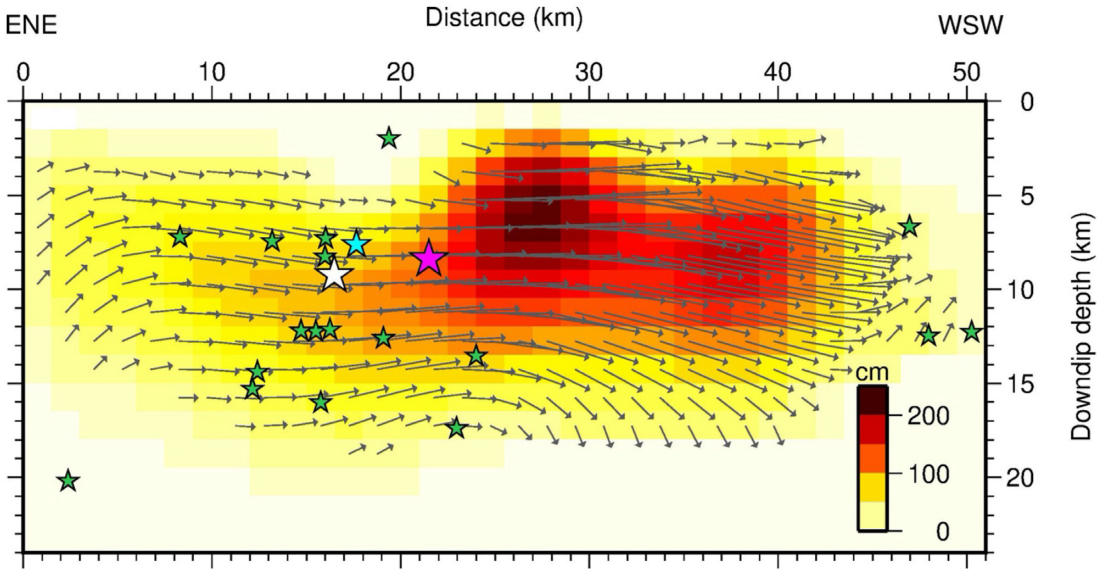


**Figure 5.** Slip distribution model on the Pütürge fault segment estimated in this study which is used in stochastic ground motion simulations. The pink and white stars represent the location of the main shock provided by AFAD and KOERI, respectively; the white blue and green stars are, respectively, the major aftershocks with $M > 5$ and $M > 4$ projected on the fault surface (within 3 km). The grey arrows indicate the estimated slip directions for each subfault.

**Table 2.** Model parameters related to source, path and site terms that are considered for the ground motion simulations for the $M_w$ 6.8 Elazığ earthquake.

| Parameters | Values | Reference |
|---|---|---|
| Fault (strike and dip) | 242°–75° | This study |
| Fault dimension | 51 × 24 km$^2$ | This study |
| Moment magnitude | 6.8 | This study |
| Depth of the top of fault plane | 0.0 km | This study |
| Subfault dimension | 1.5 × 1.5 km$^2$ | This study |
| Stress drop | 9 | This study |
| Crustal shear wave velocity ($\beta$) | 3.5 km s$^{-1}$ | Gök *et al.* (2007) |
| Crustal density | 2800 kg m$^{-3}$ | |
| Rupture velocity | 0.8×$\beta$ | |
| Pulsing area percentage | 50 per cent | Boore (2009) |
| Kappa parameter | 0.035 and 0.04 s | Boore & Joyner (1997) |
| | NEHRP generic rock and generic soil site | BSSC 2001 |
| Distance dependent of duration | 0.0 (0–10 km) | Atkinson & Boore (1995) |
| | 0.1 ($R$ > 10 km) | |
| Attenuation model, Q(f) | $100f^{0.43}$ | Akinci *et al.* (2014) |
| Geometrical spreading Coef. | $r^{-1.0}$ $r \leq 100$ km | Akinci & Antonioli (2013) |
| | $r^{-0.5}$ $r \leq 100$ km | |
| Window function | Saragoni Hart | Boore (1983) |
| Local amplification | NEHRP sites | Boore & Joyner (1997) |

therefore the potential to produce destructive earthquakes in the future.

## 3 SENTINEL-1 SAR DATA

We use SAR data acquired by the Sentinel-1 satellites in TOPS (Terrain Observation by Progressive Scans) mode, exploiting two ascending and two descending interferograms to measure the ground displacement due to the 24 January, 2020, $M_w$ 6.8 Elazığ earthquake. The epicentral area is in fact covered by four Sentinel-1 tracks: the ascending tracks 116 and 043 (Figs 2, S1 and S2), and the descending tracks 123 and 021 (Figs 3, S3 and S4). The ascending track 116 and the descending track 021 had the last pre-earthquake image acquisitions on 21 January, while the ascending track 043 and the descending track 123 on 22 January. Subsequent acquisitions were made at 6-d interval. To reduce the contribution from potential post-seismic deformation, we form the coseismic interferograms using images acquired closest to the earthquake (the first post-seismic acquisitions along the ascending track 116 and the descending track 021 were on 27 January; while for the other tracks were on 28 January).

We process the data using the Sentinel Application Platform SNAP software that is provided freely by the European Space Agency. We use precise orbit data and Shutter Radar Topography Mission 1 arcsec data (Jarvis *et al.* 2008) for the image removal of flat-earth phase and topographic phase. The resulting interferograms were then filtered by applying the Goldstein filter (Goldstein

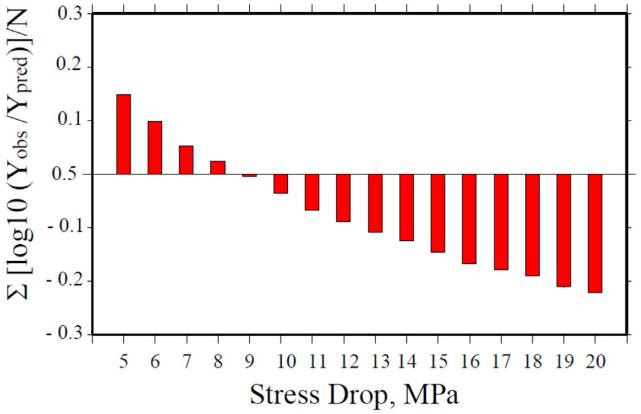


**Figure 6.** Residuals between observed and simulated PGA and PGVs calculated for sixteen drop parameters, ranging from 5 to 20 MPa, that minimize the misfit between observed and simulated ground motion.

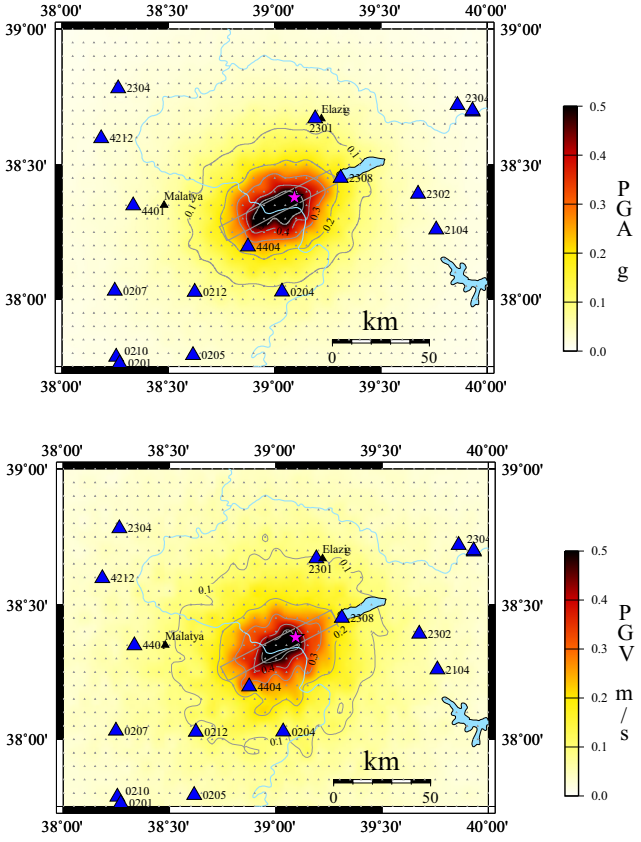


**Figure 7.** Spatial distributions of synthetics using the spectral parameters given in Table 2 in terms of (a) PGA and (b) PGV values, calculated at rock site (BC type soil classification, $V_{S30} = 760$ m s$^{-1}$), respectively. The region is divided into regular grid spacing of 5 km as indicated by small-black dots shown in figure so that the simulations are performed for the 1066 virtual stations. The grey box represents our extended fault plane solution. The pink star indicates the main shock epicentre provided by AFAD.

& Werner 1998) to reduce interferometric phase noise. Finally, we unwrapped the phase using Statistical-Cost Network-Flow Algorithm for Phase Unwrapping (SNAPHU) (Chen & Zebker 2001) and the interferograms were geocoded to obtain the ground deformation maps. Because of the intrinsic ambiguity of phase unwrapping, similarly to Wang & Burgmann (2020), we flatten the unwrapped interferograms by fitting a polynomial function to phase at pixels away from the epicentre, where the expected ground deformation is small. Unfortunately, there are no permanent GNSS (Global Navigation Satellite System) stations in the near-field of the epicentre for a direct comparison with InSAR Line-Of-Sight (LOS) displacements. In fact, the nearest GNSS station is located about 35 km from the epicentre, in Elazığ city, and has a significant static offset of only ∼3 cm towards SW (available in an open file report at https://deprem.afad.gov.tr/depremdokumanlari/1831). Nevertheless, the InSAR displacements are in good agreement with Elazığ GNSS measurements projected onto the LOS.

The ground deformation retrieved from the ascending and descending unwrapped interferograms are characterized by two ENE–WSW striking deformation lobes located on both sides of the EAFZ alignment, with maximum LOS displacement of about 25–30 cm (Figs 2 and 3). The observed differences in the ascending and descending LOS maps reveal a combination of mainly horizontal movements consistently with the strike-slip left-lateral mechanisms of the EAFZ.

## 4 FAULT GEOMETRY AND COSEISMIC SLIP

In order to image the fault geometry and slip distribution of the 2020 Elazığ main shock, we performed fault slip modelling using rectangular dislocations embedded in an elastic, homogeneous and isotropic half-space (Okada 1985), following a standard two-steps procedure (e.g. Cheloni *et al.* 2010, 2019): (1) we inverted the LOS displacements to retrieve the fault geometry and then (2) the best-fitting uniform-slip fault parameters are used as *a priori* for the estimation of the coseismic slip distribution. Before modelling, the InSAR interferograms were down-sampled using a resolution-based down-sampling scheme (Lohman & Simons 2005, Figs S1, S2, S3 and S4).

In the first step, we carried out a non-linear optimization of the fault geometry by using a simulated annealing algorithm (Corana *et al.* 1987). The best-fitting uniform slip model is described by a 242°ENE–WSW striking and 75°NW dipping strike-slip (rake about –7.5°) 32.1 km × 8.5 km fault plane passing through the hypocentral location (Fig. 4, red box) and in good agreement with focal solutions. The average uniform slip is 1.3 m, which using a value of 30 GPA for rigidity, yields an estimated seismic moment of 1.04 × $10^{19}$ Nm, equivalent to a $M_w$ 6.7 earthquake (the results of the uniform-slip model are displayed in Figs S5–S8).

In the second step, in order to estimate slip distribution on the fault plane, we extended the uniform slip fault to capture the area affected by aftershocks and subdivided the fault into small patches of constant size (1.5 km × 1.5 km). We apply positivity constraints and regularize the linear inversion by applying spatial smoothing (Fig. S9). Additional terms consisting of a linear ramp for each InSAR interferograms are also included in the inversion and relative weights were applied to properly combine the different data sets (Fig. S10).

The best-fitting slip distribution on the extended fault plane (51 km × 24 km) agrees with the distribution of aftershocks (Figs 4 and 5). The fit to the data significantly improves passing from the uniform slip to a variable slip model: from 2.75 to 1.64 cm and from 2.47 to 1.78 cm for the LOS displacements on ascending track 116 and descending track 123, respectively, and from 3.22 to 1.65 cm and from 3.14 to 1.29 cm for the LOS displacements on ascending track 043 and descending track 021, respectively (Figs 2, 3, S11

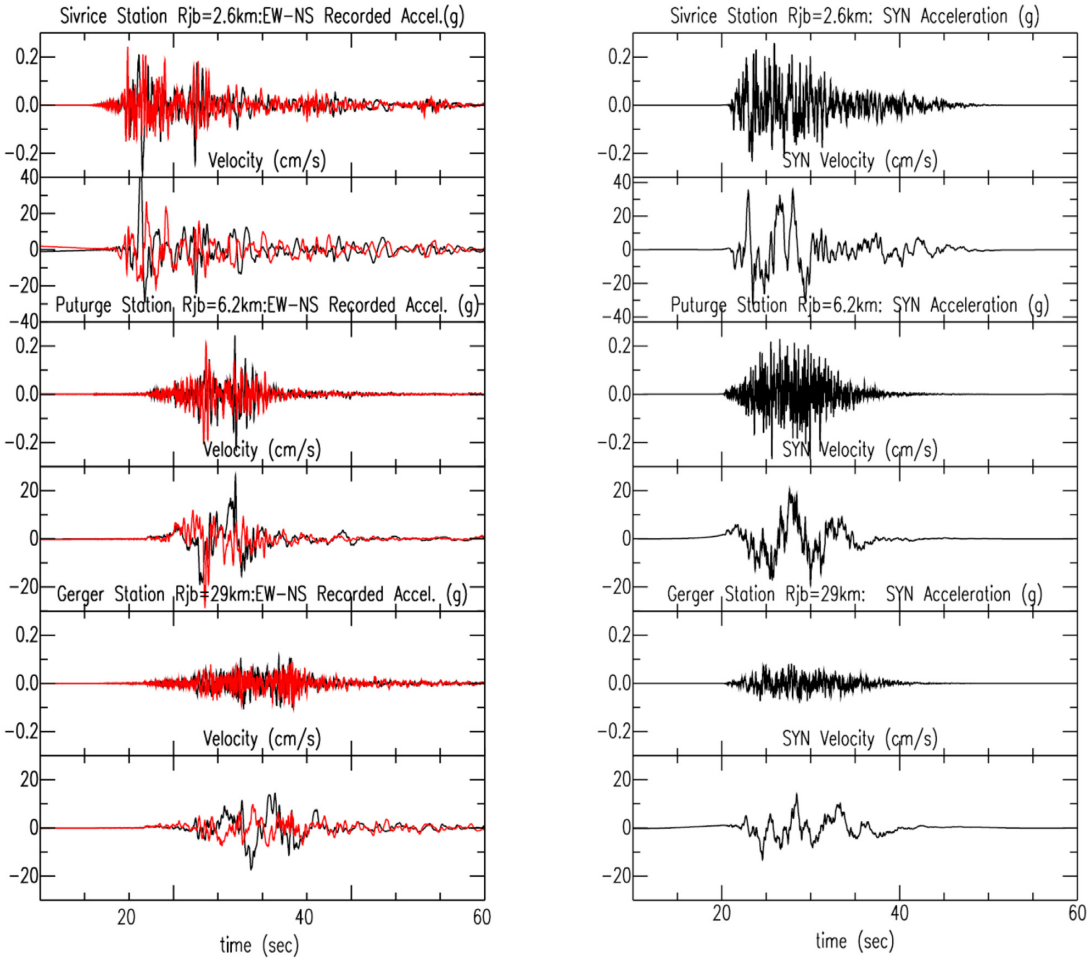


**Figure 8.** Horizontal component acceleration, and velocity time history plots at three closest stations to the fault rupture. Recorded (left-hand panels, black and red colour for two horizontal components EW and NS, respectively) and simulated (right panels) at the closest Sivrice, Pütürge, and Gerger sites to the earthquake rupture for the 2020 Elazığ $M_w$ 6.8 earthquake.

and S12). The coseismic slip distribution model shows two major asperities with peak slip of about 2–2.3 m, located WSW respect to the epicentre, and mostly confined within the first 8 km, that is roughly contained in the uniform slip fault (red box in Fig. 4), for a length of about 40 km, thus leaving unbroken the WSW part of the Pütürge fault segment. In addition, our variable slip model shows some slip also to the ENE of the epicentre, in an area where a number of $M > 4$ earthquakes occurred. The resulting total seismic moment ($1.70 \times 10^{19}$ Nm) agrees with an $M_w$ 6.8 earthquake. The rake angles of the major coseismic fault patches are consistent with a predominantly pure left-lateral strike-slip faulting mechanisms. The two main asperities characterizing our slip model agree with the up-dip rupture episodes and with the unilaterally WSW rupture directivity, as retrieved by USGS finite fault analysis (U.S. Geological Survey 2020) and by the recent study of Melgar *et al.* (2020). Our retrieved slip located ENE of the epicentre, implies instead bilateral rupture propagation.

The inversion was repeated using separately the ascending and the descending tracks, respectively. The resulting coseismic slip distribution is showed in Fig. S13. They are quite similar, showing two major coseismic slip patches located WSW of the hypocentre, suggesting these patches to be a robust feature of the retrieved slip distribution. Notwithstanding, there are some differences, in fact, the descending tracks-only inversion (Fig. S13b) appears to require a more eastward position of the smaller patch of slip located ENE of the epicentre as retrieved in the joint inversion.

## 5 STOCHASTIC MODELLING OF HIGH-FREQUENCY GROUND MOTION

In this section, we attempt to simulate the high-frequency ground motions for the $M_w$ 6.8 Elazığ earthquake using a well-known stochastic finite-fault simulation method (Motazedian & Atkinson 2005). To do so we gather several parameters related to the source, the path and the site that are essential and requested by the adopted approach have been chosen among those several existing models published for the eastern Turkey.

### 5.1 Finite-fault source model

The necessary source parameters are defined in terms of the fault geometry, rupture velocity, stress drop and seismic moment. The slip distribution along the fault plane is another crucial input parameter particularly for the ground motion simulation in the source area. The slip model determined in this study is considered as an input for our ground motion calculations. The fault plane geometry was determined from the geodetic inversion with strike 242° and dip

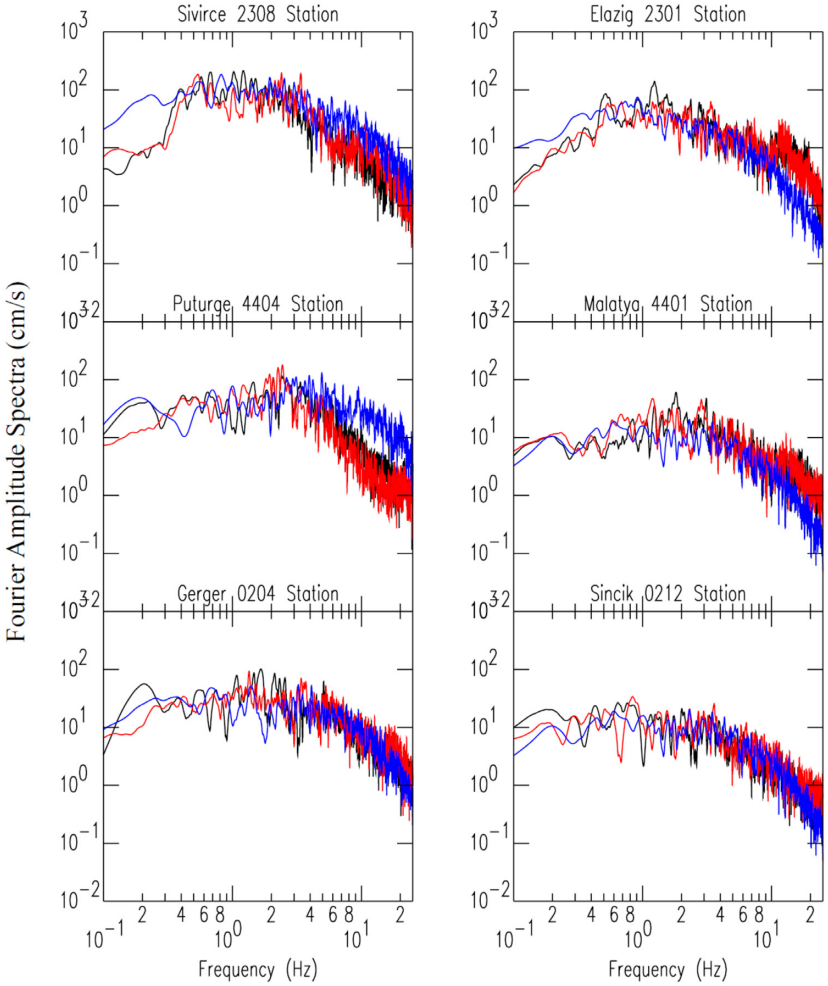


**Figure 9.** Comparison of observed and simulated Fourier amplitude spectra of acceleration (cm $s^{-1}$) at six selected stations. Simulated spectra (solid blue lines) and observed spectra for the two horizontal EW and NS components (solid red and black lines, respectively).

75° and with the top of the fault plane at 0 km depth (Fig. 5). Two patches of slip are examined over the fault plane: the larger one is located at the centre and has the highest slip of about 2.3 m and the other is located at southwestern part of the fault and has about 2 m of slip. The dimensions of the modelled left-lateral strike-slip fault plane are 50 km × 25 km and our rupture model includes 34 × 16 subfaults.

There have been several efforts to determine the fault rupture and mechanism of the 2020 Elazığ earthquake, established on various data set (teleseismic, GPS and InSAR) and alternative inversion methods (e.g. Melgar *et al.* 2020). Our inversion results agree with these models defining the location of the slip asperities on the fault plane and the quantitative description of the slip during the earthquake rupture. The parameters of the finite-fault source model used in our ground motion simulations are listed in Table 2.

### 5.2 High-frequency seismic wave attenuation model

The seismic wave propagation and the seismic attenuation is an important topic and it is essential for the prediction of earthquake ground motion in seismic hazard analysis. Determining the mechanism of attenuation helps to understand the regional differences observed on the ground motion. There have been several studies to determine the attenuation characteristics in eastern Turkey using various database and methods (Mitchell *et al.* 1997; Mitchell & Cong 1998; Zor *et al.* 2007; Pasyanos *et al.* 2009; Sertcelik 2012; Akinci *et al.* 2014).

Recently Akinci *et al.* (2014) provided a complete description of the characteristics of the source and the attenuation of the ground motion around the Lake Van region (eastern Turkey) using a large set of broadband data of the main shock and aftershocks of the 23 October 2011 $M_w$ 7.1 Van earthquake. They observed strong crustal attenuation, $Q(f) = 100f^{0.43}$ together with the geometrical spreading, $g(r)$, occurring at a hypocentral distance of 40 km which it changes from a body-wave-like function g $(r) \propto r^{-1.0}$ to a functional form g $(r) \propto r^{-0.5}$ expected for surface waves. These results are not very different from those observed by Zor *et al.* (2007) using the Lg waves through the two stations method and back projection tomography; $Q_{Lg0}$ was around 100 with its frequency dependence $n = 0.4$–$0.6$. Sertcelik (2012) has also estimated the seismic wave attenuation using the coda waves as a function of the lapse time and frequency over the EAFZ. Although those studies result with a similar $Q$ value (∼100) over the Eastern Anatolia, in our study, we decide to use most recently characterized seismic attenuation parameters as given by Akinci *et al.* (2014) (Table 2).

The geometrical spreading values governed by the crustal structure, capable of producing post-critical reflections from mid crustal

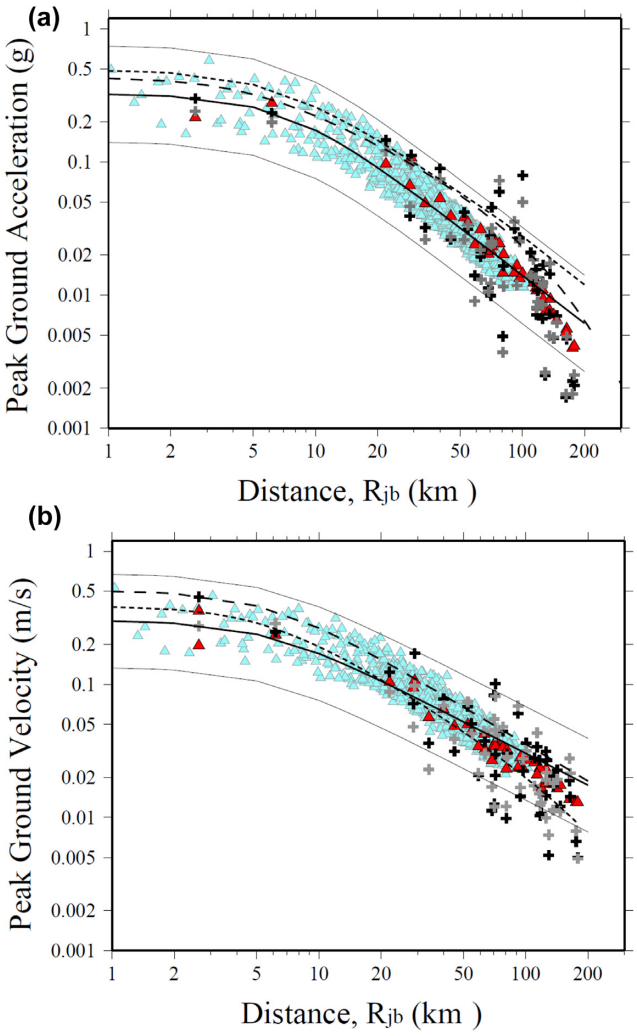


**Figure 10.** Comparisons between observed and simulated (a) peak ground acceleration, PGA and (b) peak ground velocity, PGV. The simulated values are obtained using a dynamic corner frequency approach. The PGA and PGV simulated values were estimated for an earthquake of $M_w$ 6.8 using the parameters given in Table 2 and the proposed fault geometry and slip distribution obtained in this study, for the 1066 virtual stations (light blue triangles). The black crosses represent the observed data of Elazığ earthquake recorded in two horizontal components (EW light grey and NS black coloured crosses) at 43 stations while the red triangles represent those from simulated seismograms at the same stations on a rock site, $V_{s30} = 760$ ms$^{-1}$. Ground Motion Predictions Equations (GMPEs), obtained using Boore *et al.* (2014) (short dashed line); Bindi *et al.* (2014) (long dashed line) and Akkar & Cagnan (2010) (thick solid line) and the $\pm 1\sigma$ the total standard deviation of AC10 (thin solid lines) for a rock site of $V_{s30} = 760$ m s$^{-1}$ are also shown.

and Moho discontinuities are also appropriated as given by Akinci & Antonioli (2013). The stress drop parameter $\Delta\sigma$ which governs the levels of the acceleration spectrum at high frequencies is estimated between 8 and 20 MPa by Akinci *et al.* (2006), Malagnini *et al.* (2010), Akinci & Antonioli (2013) and Akinci *et al.* (2014) for the 1999 Kocaeli, $M_w$ 7.2 earthquake with strike-slip faulting and for the 2011 Van Lake $M_w$ 7.1 earthquake with reverse faulting. Since the stress drop parameter is not estimated specifically for the $M_w$ 6.8 Elazığ earthquake, we calculate the residuals between the observed PGA and PGV values and those from simulations over 16 different stress drop parameters, from 5 to 20 MPa. Finally, we select the $\Delta\sigma$ that minimizes the misfit between the observed and simulated PGA and PGV data.

Results presented in Fig. 6 demonstrate how the choice of the stress drop parameter affects the misfit. The lowest bias determined by averaging the residuals over the 43 stations indicates the best parameter that could be considered for the simulations. The chosen stress drop parameter for our ground motion estimations that produces a good fit to the observed data for the PGA and PGV is equal to $\Delta\sigma = 9$ MPa.

## 6 HIGH FREQUANCY GROUND MOTION SIMULATIONS FOR THE $M_w$ 6.8 ELAZIG EARTHQUAKE

### 6.1 Spatial distribution of simulated ground motions

In order to investigate the spatial variation of ground motion caused by the $M_w$ 6.8 Elazığ earthquake, we calculate ground motion parameters together with the synthetic time histories at 43 recording stations, and at 1066 virtual stations on a regular grid with 5 km spacing, covering a region between 38.25–39.5°E and 38.0–38.75°N up to 200 km distances. The high frequency seismograms are generated using a stochastic finite-fault model approach, based on a dynamic corner frequency (Motazedian & Atkinson 2005; Boore 2009) and considering the spectral parameters as given in Table 2. Spatial distribution of the estimated ground motion parameters in terms of PGA and PGV values within the study area is shown in Figs 7(a) and (b), respectively.

The site-amplification effect is considered as uniform for the whole region and referred to the BC type generic rock site condition ($V_{s30} = 760$ m/s, the shear wave velocity averaged over the top 30 m of the soil, BSSC 2001). So that, the spatial distributions of PGA and PGV values mainly reflects the source effects. We observe that the largest ground shaking is concentrated along the rupture fault plane, where PGA and PGV values raising up to 0.5 g and 40 cm/s, respectively. Particularly, we observe the strongest ground shaking within the surface projection of the fault around the location of the two slip asperities; one asperity is located at the centre of the fault plane and is larger and much stronger than the second asperity that is located in the southern section of the fault plane. Finally, while the near-field results are governed by the source effects, such as the distribution of asperities on the fault plane, intermediate distances are controlled mainly by the propagation and the attenuation of seismic waves with distance. However, since the stochastic approach adopted in our study is not very sensitive to large-scale source related directivity effects, the simulated ground motion may not be suitable for producing the expected ground motion variability in the near-fault region.

Some of the simulated synthetic waveforms together with the registered seismograms are shown in Fig. 8 at three near-fault stations (Sivirce, Pütürge and Gerger). The soil conditions are provided for Sivrice, Pütürge and Gerger stations in the AFAD website. Station Sivrice (2304) located on the soil type with $V_{s30}$ ~450 m s$^{-1}$ is the closest station to the fault rupture, with Joyner and Boore distance to the fault surface of 3 km. The simulated PGA and PGV values are 328 cm s$^{-2}$ and 31 cm s$^{-1}$, computed considering the soft soil site amplifications, while the observed PGA values are 238 and 293 cm s$^{-2}$ and the observed PGV values are 27 and 45 cm s$^{-1}$ for the two horizontal components, respectively. Simulations at Pütürge station (2305) located on the rock site with a $V_{s30}$ ~1380 m s$^{-1}$ and at 6 km distance from the fault surface, result in a simulated PGA value of

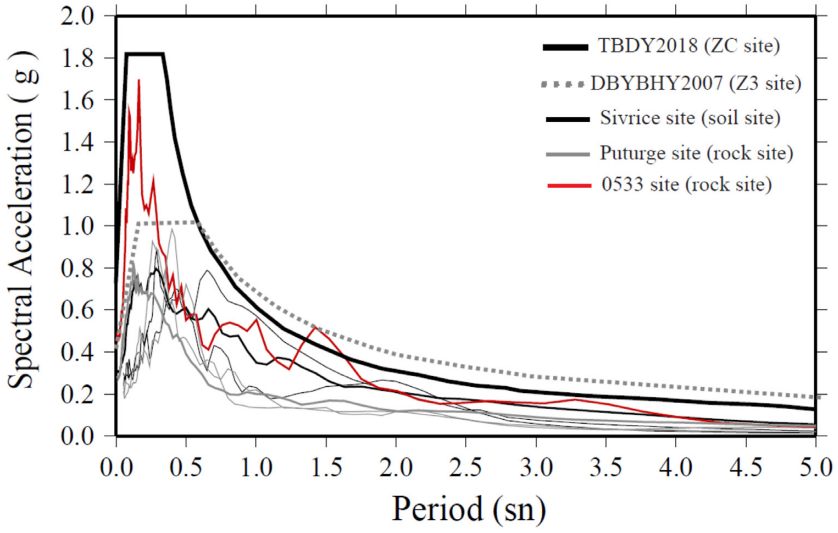


**Figure 11.** The spectral accelerations from the recorded (thin lines) and simulated (thick lines) seismograms for Sivrice, Pütürge and one for a virtual station (red colour) located close to the nucleation point where maximum slip is released over the fault rupture, and comparison with the code-based spectrum from old DBYBHY2007 and new TBDY2018 building codes, respectively.

268 cm $s^{-2}$ while the observed values are 228 and 193 cm $s^{-2}$. The simulated PGV value is instead 25 cm $s^{-1}$, while the observed values are 29 and 25 cm $s^{-1}$ for the two horizontal components (NS and EW, respectively). The site condition at the Gerger (0204) station is given as $V_{s30} = 550$ $ms^{-1}$; our simulated ground motion parameters at this site are 87.86 cm $s^{-2}$ for PGA and 10.60 cm $s^{-1}$ for PGV values, respectively, while the recorded values are 110.1–94.24 cm $s^{-2}$ and 17.1–9.71 cm $s^{-1}$ for two horizontal components, respectively. Therefore, the PGA and PGV parameters are very well reproduced by the stochastic modelling approach for short distances.

In order to show the effectiveness of our simulations to reproduce observations in frequency domain, in Fig. 9 we compare the Fourier amplitude spectra with the recorded ones at six selected strong ground motion stations. As shown in Fig. 9, simulations provide modest estimates of the general shape and amplitudes of the spectra for almost all of the stations. The misfit at Pütürge and Gerger stations, at the higher frequencies could be attributed to inaccurate site amplification function and $\kappa$ parameter adopted for those stations in our study. The synthetic spectra calculated using a high-frequency attenuation parameter $\kappa = 0.035$ s and the frequency-dependent site amplification of the BC type site classification may be insufficient to capture all the features of the spectral variation and real transfer function driven by the detailed velocity-depth profile ($V_{s30}$).

### 6.2 Comparison of observed and simulated ground motions with selected GMPEs

We validate our simulated ground motion parameters against the 43 observed PGA and PGV values up to 200 km distances from the recordings of the Elazığ earthquake (Table 1) and compare our simulations with the three selected GMPEs derived for the active shallow crustal regions. These include the GMPEs developed (1) within the context of the Next Generation Attenuation (NGA) models given by Boore *et al.* (2014) (hereafter, BSSA14); (2) from European and the Middle East strong motion database of Bindi *et al.* (2014) (hereafter, BIN14) and (3) from national strong motion database and events as the Turkish attenuation model of Akkar & Cagnan (2010, hereafter AC10).

In Fig. 10 the two horizontal components of the PGAs recorded by the total of 43 strong motion stations of Turkish network are plotted up to 200 km as a function of the distance, and compared with the values calculated from the two GMPEs, BSSA14, BIN14 and the AC10, together with our simulated PGAs. All GMPEs are derived for strike-slip faulting style and rock conditions, $V_{s30} = 760$ m $s^{-1}$. Simulations are also performed for the BC type site class, $V_{s30} = 760$ m $s^{-1}$ and $\kappa = 0.035$ s for all the sites (Boore & Joyner 1997; BSSC 2001). As can be seen from Fig. 10(a) the observed PGAs are mostly overestimated both by BSSA14 and BIN14 at all distances, while the AC10 model offers better fit to the observed and the simulated data at the rock sites. At distances greater than 100 km, the recorded PGAs decay with distance is larger than that predicted by the GMPEs.

The three GMPE models are in good agreement with the simulated and recorded PGV data at short distances although the BIN14 slightly overestimates both the recorded and the simulated data. Moreover, the observed PGVs are much scattered than the PGAs and makes ambitious to confirm the better fit with the predictions particularly at larger distances. It is interesting to note that the simulated PGA and PGV values determined using region specific parameters and regional strong motion data are in good agreement both with those estimated from the empirical Turkish GMPE model of AC10 and the simulated data at all distances.

In Fig. 11, we compare the spectral accelerations from the simulated and registered seismograms for Sivrice, Pütürge and from a virtual station close to the nucleation point (where maximum slip is released over the fault rupture), with the code-based design spectra (for Z3, $V_{s30} > 200$ m $s^{-1}$, and ZC, $V_{s30}$ 360–760 m $s^{-1}$, site classification) from both old DBYBHY2007 and new TBDY2018 (Türkiye Bina Deprem Yönetmeliği 2018) building codes, respectively. As it is seen in Fig. 11, response spectra of Pütürge and Sivrice station records are well-below the 475 yr design spectra from the new Turkish building codes (TBDY-2018), differently from the old code (DBYBHY-2007). The spectral acceleration of the virtual station (0533) over the fault rupture (where there are no strong motion registration/recordings available) is also covered by the spectra design by the new TBDY-2018. It can be observed from Fig. 11 that the Sivrice's response spectra has long periods and higher amplitudes

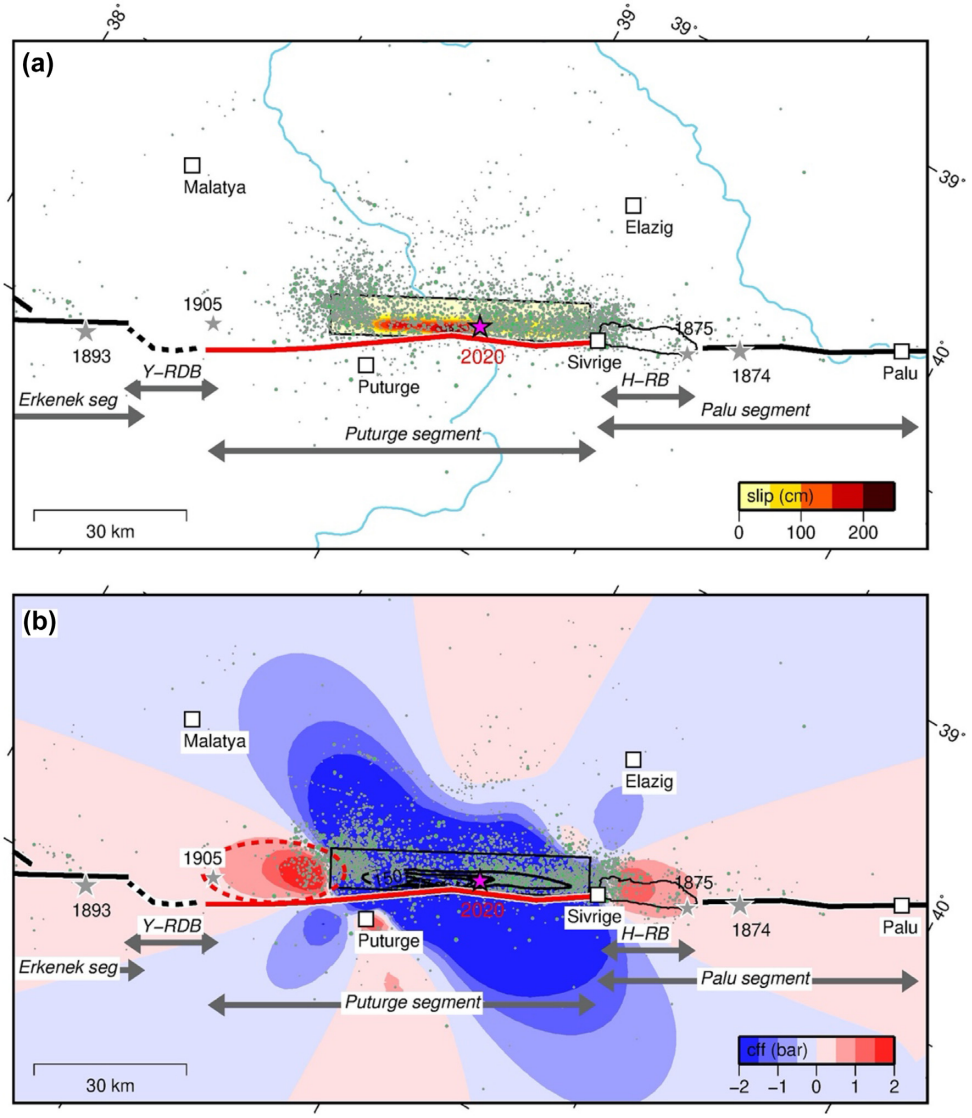


**Figure 12.** Slip distribution and Coulomb failure stress variation produced by the 24 January main shock for left-lateral ENE–WSW striking faults, in agreement with fault orientations of the EAFZ in this area. (a) Slip distribution: the green circles represent the aftershocks of the Elazig seismic sequence; pink star is the main shock epicentre provided by AFAD, while grey stars are previous large ($M > 6.6$) historical and instrumental events along the EAFZ. Solid lines represent the main fault segments, while dashed lines the fault jogs. Abbreviations: Y-RDB, Yarpuzlu restraining double bend; H-RB, lake Hazard releasing bend. The black box represents our extended fault plane solution. The main map is displayed in an oblique Mercator projection with the equator azimuth parallel to the trend of the EAFZ as in Fig. 1, (b) Change of Coulomb stress (friction coefficient = 0.4) computed at a reference depth of 10 km. The contouring (black solid lines, in cm) indicated the major coseismic slip distribution of the Elazığ earthquake. The ellipse corresponds to the slip deficit area as suggested in this study. Other symbols are as in panel (a).

due to its site characteristic when compared to that from the rock motions recorded at Pütürge.

## 7 VARIATIONS OF STATIC COULOMB STRESS IN THE STUDY AREA

It is well established that the coseismic slip causes some variations in static stress that may trigger subsequent earthquakes as well as patches of aseismic slip on unbroken portions of the causative fault itself or/and on adjacent faults (e.g. Lin & Stein 2004). In this context it is important for hazard assessment in the study area to evaluate the potential state of stress of the unruptured portions of the Pütürge segment as well as of adjacent segments following the 24 January 2020, $M_w$ 6.8 Elazığ main shock. To investigate such stress variations, we calculated the Coulomb stress change induced by the main shock using our preferred slip distribution (Fig. 12a) on fault segments having the same mechanism and geometry as the main event, and assuming an effective friction coefficient of 0.4, as is commonly used in stress interaction studies (e.g. Freed 2005; Akinci & Antonioli 2013). As expected, we find increased Coulomb stress when projected on ENE–WSW striking left-lateral slip faults at both terminations of the modelled fault plane; (1) ENE near Lake Hazar and (2) WSW of the hypocentre, respectively, in areas where also a large number of aftershocks occurred following the 24 January Elazığ earthquake (Fig. 12b).

As regard the first stressed area, this zone was likely ruptured during the 1875 earthquake. In fact, the 1875 event has been generated along the easternmost termination of the Pütürge segment (Ambraseys 1989) or within the complex releasing bend geometry that is inferred to exist within Lake Hazar (Duman & Emre 2013, H-RB in Fig. 12). Differently, the second stressed area, WSW of the hypocentre, might be a portion of the Pütürge fault segment that has not yet been broken by any seismic event in the last centuries (red ellipse in Fig. 12b). In fact, there is a debate on the exact location of the 1905 ($M_s$ 6.8) earthquake, that is the last relevant seismic event possibly located around the western end of the Pütürge segment (Ambraseys 1989). This event might have happened either on the Yarpuzlu restraining bend (Y-RDB in Fig. 12) or along the western part of the Pütürge fault segment itself. Depending of the real location of the 1905 earthquake, the first hypothesis allows the possibility that the western part of the Pütürge segment may be an unbroken area that may rupture in a future earthquake(s).

## 8 CONCLUSIONS

The 24 January 2020 $M_w$ 6.8 Elazığ earthquake in Eastern Turkey was caused by the rupture of a segment of the EAFZ, the (∼75°) NNW dipping left-lateral strike-slip Pütürge segment, which has not ruptured in the recent past and that was considered as a seismic gap prior of the 2020 seismic sequence (Duman & Emre 2013). The slip distribution obtained from the geodetic inversion shows two major asperities with peak slip of ∼2.3 m, located WSW from the epicentre, thus implying a marked westward directivity for the Elazığ main shock. The seismic moment release calculated with the geodetic data is $1.70 \times 10^{19}$ Nm (equivalent to a $M_w$ 6.8), in agreement with magnitude estimates provided by different national and international Institutes. The slip distribution along the ∼90-km-long causative Pütürge fault segment implies also that the western part of the seismogenic fault remained unruptured and was positively stressed by an increase of Coulomb stress.

We simulate the high-frequency ground motion and seismograms at 1066 virtual stations ranging between 0.1 and 100 km distances in the epicentral area to have detailed point of view on ground motion intensity distribution particularly close to the fault rupture where the maximum damaged observed. In the near-fault area we observe that our simulations have a good capability to detect near source effects and to reproduce the source complexity. The general good consistency found between synthetic and observed ground motion both in time and frequency domain, suggests the importance of the retrieving specific regional seismic parameters. We remark that ground motion parameters decay faster than the empirical ground motion equations except that of Turkish GMPEs of AC10 both at moderate and particularly at larger distance (around 100 km) this feature is captured by our simulated data. Although the adopted stochastic approach does not fully produce source directivity effects, such as coherent pulses in near-fault ground motion, it can be easily and quickly implemented for both region-specific and path-specific applications. We also demonstrate that the design spectra corresponding to 475 yr return period, provided by the new Turkish building code is not exceeded by the simulated seismograms in the epicentral area where there are no strong motion stations and no recordings available.

Finally, our preferred fault model, computed stress redistribution, and location of historical earthquakes along the EAFZ highlights some interesting features that are relevant to seismic hazard assessment in the region. In fact, to the WSW of the 2020 Elazığ seismic sequence, our fault modelling and stress calculation suggests the presence of a stressed and possibly unbroken area of the Pütürge segment that should be considered for future hazard assessment. For this reason, our results suggest that the occurrence of future significant earthquakes to the WSW of Pütürge city cannot be ruled out, and therefore a significant seismic hazard still remains in the area.

## ACKNOWLEDGEMENTS

We would like to thank the Editor, Dr Kosuke Heki, the reviewer Arben Pitarka of Lawrence Livermore National Laboratory, CA, and the reviewer Farnaz Kamranzad of University of Tehran, for their constructive suggestions, which helped to improve the manuscript. Most of the figures have been created using the Generic Mapping Tools version 4.2.1 (www.soest.hawwai.edu/gmt) and the software of Seismic Analysis Code (SAC) is used for many of the calculations throughout several set of macros. We use Copernicus Sentienel-1 InSAR imagery (https://scihub.copernicus.eu/). Sentinel-1 data are copyright of Copernicus (2020). We thank everyone at the Earthquake Department of the Disaster and Emergency Management Presidency, AFAD for making the strong motion data available (https://tadas.afad.gov.tr/).

## REFERENCES

Akinci, A, Malagnini, L., Herrmann, R.B. & Kalafat, D., 2014. High-frequency attenuation in the Lake Van Region, Eastern Turkey, *Bull. seism. Soc. Am.,* **104**(3), doi:10.1785/0120130102.

Akinci, A. & Antonioli, A., 2013. Observations and stochastic modelling of strong ground motions for the 2011 October 23 Mw 7.1 Van, Turkey, earthquake, *Geophys. J. Int.,* **192,** doi:10.1093/gji.ggs075.

Akinci, A., Aochi, H., Herrero, A., Pischiutta, M. & Karanikas, D., 2017. Physics-based broadband ground-motion simulations for probable Mw ≥7.0 earthquakes in the Marmara Sea Region (Turkey), *Bull. Seismol. Soc. Am,* **107**(3), doi:10.1785/0120160096.

Akinci, A., Malagnini, L., Herrmann, R.B., Gok, R. & Sorensen, M.B., 2006. Ground motion scaling in Marmara region, Turkey, *Geophys. J. Int.,* **166,** 635–651.

Akkar, S. & Cagnan, Z., 2010. A local ground-motion predictive model for Turkey and its comparison with other regional and global ground-motion models, *Bull. seism. Soc. Am.,* **100,** 2978–2995.

Aktug, B., Ozener, H., Dogru, A., Sanbucu, A., Turgut, B., Halicioglu, K., Yilmaz, O. & Havazli, E., 2016. Slip rates and seismic potential on the East Anatolian Fault System using an improved GPS velocity field, *J. Geod.,* **94–95,** 1–12.

Ambraseys, N., 2009. *Earthquakes in the Mediterranean and Middle East: A Multidisciplinary Study of Seismicity up to 1900*. Cambridge Univ. Press, 968pp.

Ambraseys, N.N., 1989. Temporary seismic quiescence: SE Turkey, *Geophys. J. Int.,* **96,** 311–331.

Ambraseys, N.N. & Jackson, J.A., 1998. Faulting associated with historical and recent earthquakes in the Eastern Mediterranean region, *Geophys. J. Int.,* **133,** 390–406.

Atkinson, G.M. & Boore, D.M., 1995. Ground-motion relations for eastern North America, *Bull. seism. Soc. Am.,* **85,** 17–30.

Barka, A.A. & Kandinsky-Cade, K., 1988. Strike-slip fault geometry in Turkey and its influence in earthquake activity, *Tectonics,* **7,** 663–684.

Bindi, D., Massa, M., Luzi, L., Ameri, G., Pacor, F., Puglia, R. & Augliera, P., 2014. Pan-European ground motion prediction equations for the average horizontal component of PGA, PGV and 5%-damped PSA at spectral periods of up to 3.0 s using the RESORCE dataset, *Bull. Earthq. Eng.,* **12**(1), 391–340

Boore, D.M., 1983. Stochastic simulation of high-frequency ground motions based on seismological models of the radiated spectra, *Bull. seism. Soc. Am.,* **73,** 1865–1894.

Boore, D.M., 2003. Simulation of ground motion using the stochastic method, *Pure appl. Geophys.,* **160,** 635–676.

Boore, D.M., 2009. Comparing stochastic point-source and finite-source ground-motion simulations: SMSIM and EXSIM, *Bull. seism. Soc. Am.,* **99,** doi:10.1785/0120090056.

Boore, D.M. & Joyner, W.B., 1997. Site amplifications for generic rock sites, *Bull. seism. Soc. Am.,* **87,** 327–341.

Boore, D.M., Stewart, P.J., Seyhan, E. & Atkinson, G.M., 2014. NGAWest2 equations for predicting PGA, PGV, and 5% damped PSA for shallow crustal earthquakes, *Earthq. Spectra,* **30**(3), 1057–1085.

BSSC (Building Seismic Safety Council), 2001. NEHRP recommended provisions for seismic regulations for new buildings, and other structures, 2000 Edition. *Part 1: Provisions, Building Seismic Safety Council for the Federal Emergency Management Agency (Report FEMA368),* Washington, DC, USA.

Cetin, H., Guneyli, H. & Mayer, K., 2003. Paleoseismology of the Palu-Lake Hazar segment of the East Anatolian Fault Zone, Turkey, *Tectonophysics,* **374,** 163–197.

Cheloni, D. *et al.*, 2010. Coseismic and initial post-seismic slip of the 2009 Mw 6.3 L'Aquila earthquake, Italy, from GPS measurements, *Geophys. J. Int.,* **181**(3), 1539–1546.

Cheloni, D. *et al.*, 2019. Heterogeneous Behavior of the Campotosto Normal Fault (Central Italy) Imaged by InSAR GPS and Strong-Motion Data: Insights from the 18 January 2017 Events, *Remote Sens.,* **11,** 1482.

Chen, C.W. & Zebker, H.A. 2001. Two-dimensional phase unwrapping with use of statistical models for cost functions in nonlinear optimization, *J. Opt. Soc. Am.,* **18**(2), 338–351.

Corana, A., Marchesi, M., Martini, C. & Ridella, S., 1987. Minimizing multimodal functions of continuous variables with the "Simulated Annealing" algorithm, *ACM Trans. Math. Softw.,* **13,** 262–280.

Duman, T.Y. & Emre, Ö., 2013. The East Anatolian Fault: geometry, segmentation and jog characteristics, *Geol. Soc., Lond., Spec. Publ.,* **372,** 495–529.

Freed, T.G., 2005. Earthquake triggering by static, dynamic, and post-seismic stress transfer, *Annu. Rev. Earth Planet Sci.,* **33,** doi:10.1146/annurev.earth.33.092203.122505.

Goldstein, R.M. & Werner, C.L., 1998. Radar interferograms filtering for geophysical applications, *Geophys. Res. Lett.,* **25,** 4035–4038.

Graves, R. & Pitarka, A., 2010. Refinements to the Graves and Pitarka (2010) broadband ground motion simulation method, *Seismol. Res. Lett.,* **86**(1), 75–80.

Gök, R., Pasyanos, M.E. & Zor, E., 2007. Lithospheric structure of the continent collision zone: Eastern Turkey, *Geophys. J. Int.,* **169,** 3, 1079–1088.

Hempton, M.R., Dewey, J.F. & Saroglu, F., 1981. The East Anatolian transform fault: along strike variations in geometry and behavior, *EOS, Tran. Am. Geophys. Un., EOS,* **62,** 393.

Herece, E., 2008. *Dogu Anadolu Fayi (DAF) Atlasi*. General Directorate of Mineral Research and Exploration. Special Publications, Ankara, Serial Number, **14,** 359.

Irikura, K. & Miyake, H., 2011. Recipe for predicting strong ground motion from crustal earthquake scenarios, *Pure appl. Geophys.,* **168,** 85–104.

Jarvis, A., Reuter, H.I., Nelson, A. & Guevara, E., 2008. Hole-filled SRTM for the globe, version4, *CGIAR-CSI SRTM 90m Database,* available at http://srtm.csi.cgiar.org.

Karabacak, V., Onder, Y., Altunel, E., Yalciner, C.C., Akyuz, H.S. & Kiyak, N.G., 2011. Dogu Anadolu Fay Zonunun guney bati uzaniminin paleosismolojisi ve ilk kayma hizi. *Proceeding of the Aktif Tektonik Arastirma Grubu Onbesinci Calistayi (ATAG-15),* 19–22 Ekim 2011, Cukurova Universitesi, Karatas-Adana, 17.

Kondorskaya, N.V. & Ulomov, V.I., 1999. Special catalogue of earthquakes of the Northern Eurasia (SECNE). http://www.seismo.ethz.ch/static/gshap/neurasia/nordasiacat.txt.

Lin, J. & Stein, R.S., 2004. Stress triggering in thrusts and subduction earthquakes, and stress interaction between the southern San Andreas and nearby thrust and strike-slip faults, *J. geophys. Res.,* **109**(B02303), doi:10.1029/2003JB002607.

Lohman, R.B. & Simons, M., 2005. Some thoughts on the use of InSAR data to constrain models of surface deformation: noise structure and data downsampling, *Geochem. Geophys. Geosyst.,* **6**(Q01007), doi:10.1029/2004GC000841.

Mai, P.M., Imperatori, W. & Olsen, K.B., 2010. Hybrid broadband ground motion simulations: combining long-period deterministic synthetics with high-frequency multiple S-to-S backscattering, *Bull. seism. Soc. Am.,* **100**(5A), 2124–2142.

Malagnini, L., Nielsen, S., Mayeda, K. & Boschi, E., 2010. Energy radiation from intermediate to large magnitude earthquakes: implications for dynamic fault weakening, *J. geophys. Res.,* **115**(B6), doi:10.1029/2009JB006786.

McClusky, S. *et al.*, 2000. GPS constraints on plate motions and deformation in the Eastern Mediterranean: implications for plate dynamics, *J. geophys. Res.,* **105,** 5695–5719.

McKenzie, D.P., 1972. Active tectonics of the Mediterranean region, *Geophys. J. R. astr. Soc.,* **30,** 109–185.

Melgar, D., *et al.*,, 2020. Rupture kinematics of January 24, 2020 *Mw 6.7* Doğanyol-Sivrice, Turkey, earthquake on the East Anatolian Fault Zone imaged by space geodesy, *Geophys. J. Int.* , ggaa345, doi:10.1093/gji/ggaa345 .

Mena, B., Dalguer, L.A. & Mai, P.M., 2012. Pseudodynamic source characterization for strike slip faulting including stress heterogeneity and super-shear ruptures, *Bull. seism. Soc. Am.,* **102**(4), 1654–1680.

Mitchell, B. & Cong, L., 1998. Lg coda Q and its relation to the structure and evolution of continents: a global perspective, *Pure appl. Geophys.,* **153,** 655–663.

Mitchell, B.J., Pan, Y., Xie, J. & Cong, L., 1997. Lg coda Q variation across Eurasia and its relation to crustal evolution, *J. geophys. Res.,* **102,** 22767–22779.

Motazedian, D. & Atkinson, G.M., 2005. Stochastic finite-fault 800 modelling based on a dynamic 801 corner frequency, *Bull. seism. Soc. Am.,* **95,** 995–1010.

Nalbat, S.S., McCluskey, J., Steacy, S. & Barka, A.A., 2002. Stress accumulation and increased seismic risk in eastern Turkey, *Earth. Planet. Sci. Lett.,* **195,** 291–298.

Okada, Y., 1985. Surface deformation due to shear and tensile faults in a half-space, *Bull. seism. Soc. Am.,* **75,** 1135–1154.

Pasyanos, M.E., Matzel, E.M., Walter, W.R. & Rodgers, A.J., 2009. Broadband Lg attenuation modeling in the Middle East, *Geophys. J. Int.,* **177,** 1166–1176.

Pitarka, A., Graves, R., Irikura, K., Miyake, H. & Rodgers, A., 2017. Performance of Irikura recipe rupture model generator in earthquake ground motion simulations with graves and Pitarka hybrid approach, *Pure appl. Geophys.,* **174**(9), doi:10.1007/s00024-017-1504-3.

Pitarka, A., Graves, R., Irikura, K., Miyakoshi, K. & Rodgers, A., 2019. Kinematic rupture modeling of ground motion from the M7 Kumamoto, Japan, Earthquake, *Pure appl. Geophys.,* **177,** 2199–2221.

Reilinger, R. *et al.*, 2006. GPS constraints on continental deformation in the Africa-Arabia-Eurasia continental collision zone and implications for the dynamics of plate interactions, *J. geophys. Res.,* **111**(B05411), doi:10.1029/2005JB004051.

Saroglu, F., Emre, O. & Kuscu, O., 1992. The East Anatolian fault zone of Turkey, *Ann. Tecton.,* **6,** 99–125.

Sertcelik, F., 2012. Estimation of coda wave attenuation in the east Anatolia fault zone, Turkey, *Pure appl. Geophys.,* **169**(7), 1189–1204.

Seyrek, A., Demir, T., Pringle, M.S., Yurtem, S., Westway, R.W.C., Beck, A. & Rowbotham, G., 2007. Kinematics of the Amos Fault, southern Turkey, from Ar/Ar dating of offset Pleistocene basalt plates, in *Tectonics of Strike-Slip Restraining and releasing Bends,* Vol. **290,** pp. 255–284, eds Cunningham, W.D. & Mann, P., Geological Society London Special Publications.

Taymaz, T., Eyidogan, H. & Jackson, J., 1991. Source parameters of large earthquakes in the East Anatolian Fault Zone (Turkey), *Geophys. J. Int.,* **106,** 537–550.

Türkiye Bina Deprem Yönetmeliği (TBDY), 2018. *T.C. Başbakanlık Afet ve Acil Durum Yönetimi Başkanlığı, Deprem Dairesi Başkanlığı,* http://www.deprem.afad.gov.tr, Ankara.

U.S. Geological Survey, 2020. *Earthquake Hazards Program,* available at: https://earthquake.usgs.gov/earthquakes/eventpage/us60007ewc/; last accessed on 20 April 2020.

Wang, K. & Burgmann, R., 2020. Co- and postseismic deformation due to the 2019 Ridgecrest earthquake sequence constrained by Sentinel-1 and COSMO-SkyMed Data, *Seismol. Soc. Lett.,* **91**(4), 1998-2009, doi:10.1785/0220190299.

Zor, E., Sandvol, E., Xie, J., Turkelli, N., Mitchell, B., Gasanov, A.H. & Yetirmishli, G., 2007. Crustal attenuation within the Turkish Plateau and surrounding regions, *Bull. seism. Soc. Am.,* **97,** 151–161.

## SUPPORTING INFORMATION

Supplementary data are available at *GJI* online.

**Figure S1.** Downsampling of the Sentinel-1 ascending track 116 LOS coseismic displacements using a resolution-based downsampling scheme: (a) input full unwrapping interferogram; (b) resampled interferogram. Squares indicate areas within which the LOS displacements are averaged. (c) LOS profile across sections A–A' showing the full unwrapped interferogram (coloured circles) versus the resampled one (open circles). The pink star is the main shock epicentre provided by AFAD.

**Figure S2.** Downsampling of the Sentinel-1 ascending track 043 LOS coseismic displacements using a resolution-based downsampling scheme: (a) input full unwrapping interferogram; (b) resampled interferogram. Squares indicate areas within which the LOS displacements are averaged. (c) LOS profile across sections A–A' showing the full unwrapped interferogram (coloured circles) versus the resampled one (open circles). The pink star is the main shock epicentre provided by AFAD.

**Figure S3.** Downsampling of the Sentinel-1 descending track 123 LOS coseismic displacements using a resolution-based downsampling scheme: (a) input full unwrapping interferogram; (b) resampled interferogram. Squares indicate areas within which the LOS displacements are averaged. (c) LOS profile across sections A–A' showing the full unwrapped interferogram (coloured circles) versus the resampled one (open circles). The pink star is the main shock epicentre provided by AFAD.

**Figure S4.** Downsampling of the Sentinel-1 descending track 021 LOS coseismic displacements using a resolution-based downsampling scheme: (a) input full unwrapping interferogram; (b) resampled interferogram. Squares indicate areas within which the LOS displacements are averaged. (c) LOS profile across sections A–A' showing the full unwrapped interferogram (coloured circles) versus the resampled one (open circles). The pink star is the main shock epicentre provided by AFAD.

**Figure S5.** (a) Data, (b) model and (c) residuals sampled points from the unwrapped ascending track 116 interferogram. The violet box represents our best-fitting uniform-slip solution. The pink star is the main shock epicentre provided by AFAD.

**Figure S6.** (a) Data, (b) model and (c) residuals sampled points from the unwrapped ascending track 043 interferogram. The violet box represents our best-fitting uniform-slip solution. The pink star is the main shock epicentre provided by AFAD.

**Figure S7.** (a) Data, (b) model and (c) residuals sampled points from the unwrapped descending track 123 interferogram. The violet box represents our best-fitting uniform-slip solution. The pink star is the main shock epicentre provided by AFAD.

**Figure S8.** (a) Data, (b) model and (c) residuals sampled points from the unwrapped descending track 021 interferogram. The violet box represents our best-fitting uniform-slip solution. The pink star is the main shock epicentre provided by AFAD.

**Figure S9.** Trade-off curve between solution roughness and weighted misfit. The red circle indicates the chosen scalar smoothing factor.

**Figure S10.** Relationship between RMS data reduction and relative weighting factors. (a) The blue circles represent the RMS reduction of the descending track 123, while the red ones are relevant to the ascending track 116. (b) The green circles represent RMS reduction of the ascending track 043 relative to both the descending track 123 (blue circles) and the ascending track 116 (red circles). (c) The light blue circles show the RMS reduction of the descending track 021 relative to all the other data sets.

**Figure S11.** (a) Data, (b) model and (c) residuals sampled points from the unwrapped ascending track 043 interferogram. The pink star is the main shock epicentre provided by AFAD.

**Figure S12.** (a) Data, (b) model and (c) residuals sampled points from the unwrapped descending track 021 interferogram. The pink star is the main shock epicentre provided by AFAD.

**Figure S13.** Coseismic slip distributions on the causative fault segment from the inversion of (a) only the ascending tracks, (b) only the descending tracks, and (c) the full data sets. The pink star is the main shock epicentre provided by AFAD.

Please note: Oxford University Press is not responsible for the content or functionality of any supporting materials supplied by the authors. Any queries (other than missing material) should be directed to the corresponding author for the paper.